International Symposium
On Turbulence and Shear Flow
Phenomena (TSFP-9)
June 30 - July 3, 2015 *Melbourne, Australia*

DNS OF A FULLY DEVELOPED TURBULENT POROUS CHANNEL FLOW BY THE LATTICE BOLTZMANN METHOD

Y.Kuwata, K.Suga
Department of Mechanical Engineering,
Osaka Prefecture University,
1-1, Gakuen-cho, Naka-ku, Sakai 599-8531, Japan
kuwata@htlab.me.osakafu-u.ac.jp
suga@me.osakafu-u.ac.jp

ABSTRACT

To understand the turbulent flow physics over permeable porous surfaces, a direct numerical simulation (DNS) of a turbulent channel flow over a porous layer is performed by the D3Q27 multiple-relaxation time lattice Boltzmann method. The bulk mean Reynolds number is 3000 and the presently considered porous layer, whose porosity is 0.71, consists of staggered cube arrays. Using the DNS results, the phenomenological discussions through the two-point autocorrelation, one-dimensional energy spectrum and proper orthogonal decomposition (POD) analyses are carried out. The reason why the streaky structure over the porous layer becomes shorter, wider and obscurer than that near the solid wall are discussed. It is found that the low wavenumber turbulence is enhanced over the porous layer. This low wavenumber large-scale motions are considered to stem from the Kelvin-Helmholtz instability due to the weakened wall-blocking effect and the strong shear over the porous layer.

BACKGROUND

Due to its high heat and mass transfer efficiency, porous structures commonly play important role in industrial fields and thus understanding and modelling the flows over porous media are industrially crucial issues. To understand the turbulent flow physics over permeable porous surfaces, partially direct numerical simulations (DNSs) of turbulent channel flows over porous layers were performed by Breugem et al.(2006). Although they solved the turbulent flows directly in the clear channel region, they applied the volume averaged momentum equation to the porous regions. Since their simulations did not take account of the influence of not only the porous structure but also the dispersion, the predicted turbulence phenomena around and inside the porous layers might not be exactly correct. Recently, Chandesris et al. (2013) performed a full DNS study for a low Prandtl number (Pr=0.1) heat transfer field with the same flow conditions as those of Breugem et al. (2006). Although they resolved the model porous structure, it was an unrealistically revitating structure. Since their focus was on heat transfer, they did not provide further information on the turbulent flow physics than that by Breugem et al. (2006). The turbulent porous channel flows were also investigated experimentally by Suga et al.(2010 and 2011), however, due to the difficulty of the measurements inside the porous media, the measurements were limited to the clear channel regions. Accordingly, as far as the authors know, there is no study on the precise turbulence structure in the interface region over the porous layer. Therefore in this study, a DNS study of a turbulent channel flow over a porous layer is performed. To directly treat the porous structure, the D3Q27 multiple relaxation time lattice Boltzmann method of Suga et al.(2015) is employed.

NUMERICAL SCHEME

The present DNS is performed by the D3Q27 multiple relaxation time lattice Boltzmann method (MRT-LBM) (Suga et al.,2015) whose time evolution equation is

$$\begin{aligned} &|\boldsymbol{f}(\boldsymbol{x}+\xi_\alpha\delta t, t+\delta t)\rangle - |\boldsymbol{f}(\boldsymbol{x},t)\rangle \\ &= -\boldsymbol{M}^{-1}\hat{\boldsymbol{S}}\left[|\boldsymbol{m}(\boldsymbol{x},t)\rangle - |\boldsymbol{m}^{eq}(\boldsymbol{x},t)\rangle\right], \end{aligned} \tag{1}$$

where the notations such as $|\boldsymbol{f}\rangle$ is $|\boldsymbol{f}\rangle = (f_0, f_1, \cdots, f_{26})^T$, δt is the time step and ξ_α is the discrete velocity. The transformation matrix $\boldsymbol{M}$ is a 27×27 matrix which linearly transforms the distribution functions to the moments as $|\boldsymbol{m}\rangle = \boldsymbol{M}|\boldsymbol{f}\rangle$. The collision matrix $\hat{\boldsymbol{S}}$ is diagonal:

$$\begin{aligned} &\hat{\boldsymbol{S}} \equiv diag(0,0,0,0,s_4,s_5,s_5,s_7,s_7,s_7,s_{10},s_{10},s_{10},s_{13}, \\ &s_{13},s_{13},s_{16},s_{17},s_{18},s_{20},s_{20},s_{20},s_{23},s_{23},s_{23},s_{26}). \end{aligned} \tag{2}$$

The relaxation parameters presently applied are from Suga et al.(2015) as

$$\begin{aligned} &s_4 = 1.54,\ \ s_5 = s_7,\ \ s_{10} = 1.5,\ \ s_{13} = 1.83,\ \ s_{16} = 1.4, \\ &s_{17} = 1.61,\ \ s_{18} = s_{20} = 1.98,\ \ s_{23} = s_{26} = 1.74. \end{aligned} \tag{3}$$

The kinematic fluid viscosity ν is related to the relaxation parameter s_5,

$$\nu = c_s^2\left(\frac{1}{s_5}-\frac{1}{2}\right)\delta t, \tag{4}$$

where $c_s/c = 1/\sqrt{3}$ and $c = \Delta/\delta t$ where Δ is the lattice spacing. For the other details, see Suga et al.(2015).

To reduce the computational costs, the multi-block method proposed by Dupuis et al. (2003) is modified and employed in this study. To take account of the continuity of

the mass, momentum and stress tensor at the fine and coarse block boundaries, the distribution functions of the equilibrium $\boldsymbol{f}^{eq}$ and non-equilibrium $\boldsymbol{f}^{neq}$ components are imposed as

$$\boldsymbol{f}^{eq,c} = \boldsymbol{f}^{eq,f}, \tag{5}$$

$$\boldsymbol{f}^{neq,c} = \frac{s_{5,f}\Delta_c}{s_{5,c}\Delta_f}\boldsymbol{f}^{neq,f}, \tag{6}$$

where, super- and sub-scripts c and f denote the value of the coarse and fine grids, respectively.

1 FLOW GEOMETRY AND COMPUTATIONAL CONDITIONS

Figure1 illustrates the porous-walled channel geometry. The channel bottom wall is made of a porous medium whilst the solid smooth top wall is considered. The porous medium presently considered consists of staggered cube arrays and its porosity is $\varphi = 0.71$ in the homogeneous region. The permeability is obtained from the computation as $K/h^2 = 1.9\times10^{-4}$. The computational domain is $2\pi H(x)\times(H+h)(y)\times\pi H(z)$ where H is the clear channel height, the porous layer thickness is $h = 0.54H$, the cube size is $D = 0.16H$ and the cube pitch $L = 0.24H$. Hence, 5560 cubes are resolved in total. Using the modified multi-block method, the computational domain is decomposed to the finer and coarser resolution domains. The finer mesh domain mainly covers inside and around the porous layer whilst the coarser mesh domain covers the clear channel region. The grid node number of the finer and coarser mesh regions are $1674(x)\times210(y)\times837(z)$ and $837(x)\times100(y)\times419(z)$, respectively. The resolutions of the finer and coarser domains normalized by the friction velocity at the top solid wall u_τ^t are $\Delta_f^+ = 0.8, \Delta_c^+ = 1.6$, respectively. Hence the cube size D is resolved by 22 nodes. Periodic boundary conditions are applied to the spanwise direction and a pressure difference is imposed in the streamwise direction. For non-slip boundaries, which are applied to the surfaces of the top wall and the porous elements, the half-way bounce-back method is used whilst the slip boundary condition is imposed on the very bottom face of the domain. The bulk Reynolds number is $\mathrm{Re}_b = U_b H/\nu = 3000$, the permeability Reynolds number $\mathrm{Re}_K = u_\tau^p\sqrt{K}/\nu = 7.1$, the friction Reynolds numbers on the solid and porous walls

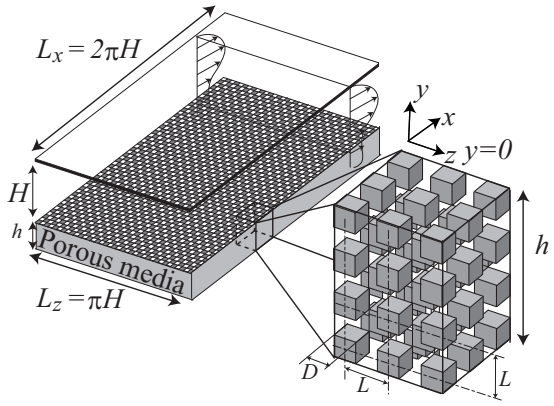

Figure 1. Computational geometry of a porous channel flow.

are $\mathrm{Re}_\tau^t = u_\tau^t\delta_t/\nu = 58$ and $\mathrm{Re}_\tau^p = u_\tau^p\delta_p/\nu = 242$. Here, δ_t and δ_p are the distances from the porous and solid walls to the location where the Reynolds shear stress becomes zero: $\delta_t = (u_\tau^t)^2/((u_\tau^t)^2+(u_\tau^p)^2)$ and $\delta_p = (u_\tau^p)^2/((u_\tau^p)^2+(u_\tau^p)^2)$, respectively. In the following discussions, the value with the superscripts " $t+$ " and " $p+$ " indicate the values normalized by the u_τ^t and u_τ^p.

RESULTS AND DISCUSSIONS

Figures 2 and 3 show the mean velocity and Reynolds stress profiles which are averaged in the $x-z$ plane. Note that y' indicates the distance from the top solid wall. As in the previous reports in the literature, Figures 2(a) and 3(a) show that the mean velocity profile becomes asymmetry due to the enhanced Reynolds shear stress near the porous layer. As shown in figure 2(b), the profiles of U^{t+} and U^{p+} near the solid wall and the porous layer are completely different and the mean velocity profile near the porous layer is much smaller than that near the solid wall. Figure 3 indicates that Reynolds stresses of the spanwise and wall-normal components near the porous layer are significantly enhanced whilst that of the streamwise component is not. Consequently the anisotropy of the Reynolds stresses near the porous layer becomes weaker. Inside the porous layer $(-0.2 < y/h < 0)$ it is confirmed that the streamwise Reynolds stress component decays most rapidly and the wall-normal component becomes the largest component. The normal stresses exist even inside the porous layer $(-0.4 < y/h < 0)$ where the Reynolds shear stress vanishes. All the presented statistical results are consistent with those in the literature. In order to understand why those statistical results are obtained from

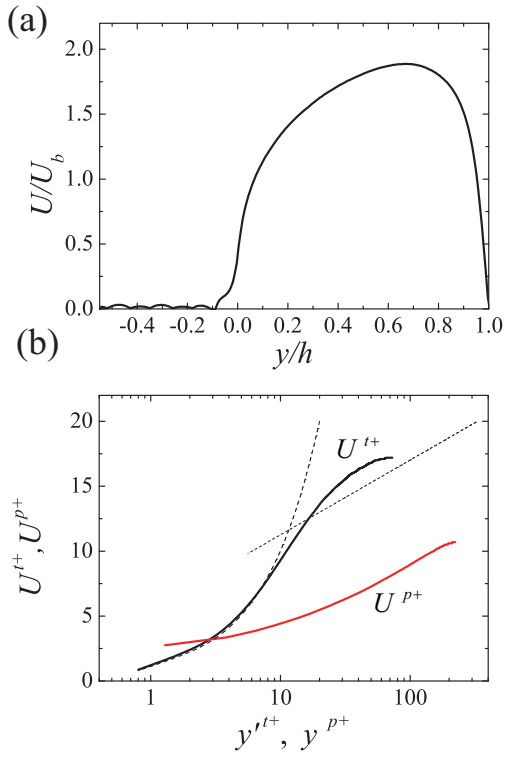

Figure 2. Mean velocity distributions: (a) normalized profile by the bulk velocity, (b) normalized profiles by the friction velocities.

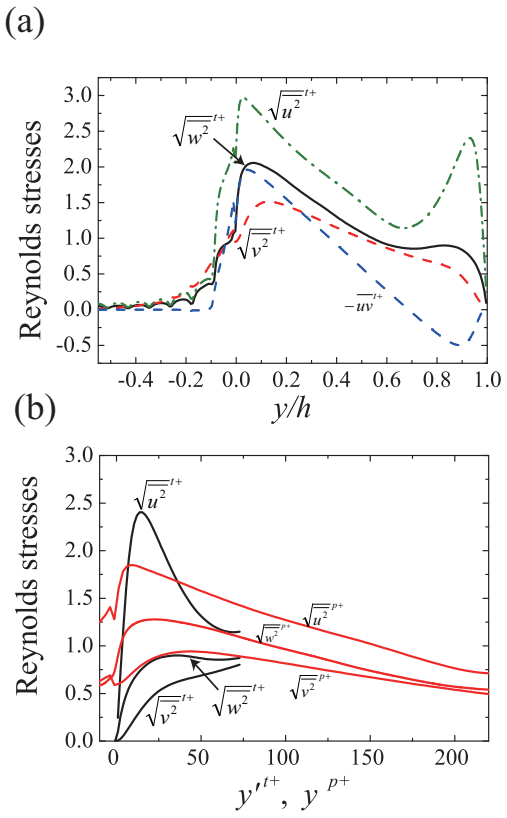

Figure 3. Reynolds stress profiles: (a) normalized profile by the solid wall friction velocity, (b) normalized near wall profiles.

the phenomenological viewpoint, the following discussions focus on the turbulent flow physics by the autocorrelation, spectrum and POD analyses.

Figure 4 shows iso-surfaces of the second invariant of the velocity gradient tensor at $Q^{t+} = 0.1$ which are coloured based on the local values of the streamwise vorticity of $-1/3 < \omega_x^{t+} < 1/3$. It clearly indicates the strong vortex motions near the porous layer. Compared with the structure near the solid wall, the vortex structure near the porous layer looks significantly disordered and the vortices penetrate into the porous layer reaching to the second cube array

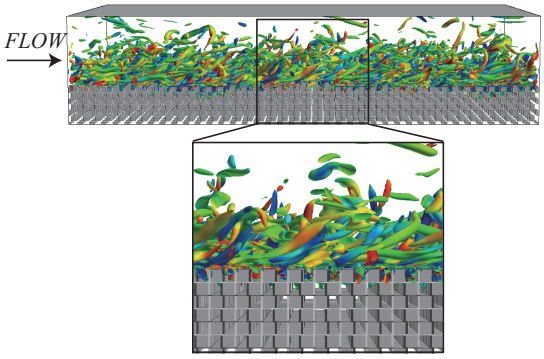

Figure 4. Second invariant of the velocity gradient tensor $Q^{+} = 0.1$ coloured by the streamwise vorticity; blue-red correspond to $-1/3 < \omega_x^{+} < 1/3$

at most. This corresponds to that the wall-normal Reynolds stress component keeps its strength up to $y/h = -0.3$ as seen in figure 3(a).

Figure 5 shows snapshots of the wall-normal vorticity ω_y at different $x-z$ planes. The vorticity of the solid and porous walls are normalized by the friction velocity on the solid wall and the porous layer, respectively. From figure 5(b), although the strong level of the vorticity is observed near the porous layer at $y^{p+} = 10$, the obvious streaks seem not to be kept. It is clear that the turbulence structure is totally different from that near the solid top wall where the elongated streaky structure can be seen in figure 5 (a). This observation is consistent with the report by Breugem et al.(2006). At the interface shown in figure 5(c), the vorticity distribution seems to be disrupted into the fine scale motions by the structural elements. Inside the porous layer shown in figure 5(d), some large scale intermittent motions which are considered to be caused by the Kelvin–Helmholtz (K-H) instability are seen. This implies that the large scale motions induced by the K-H instability at the interface carry the fine scale motions into the porous structure. Then, those fine motions dissipate there whilst the large scale motions still remain.

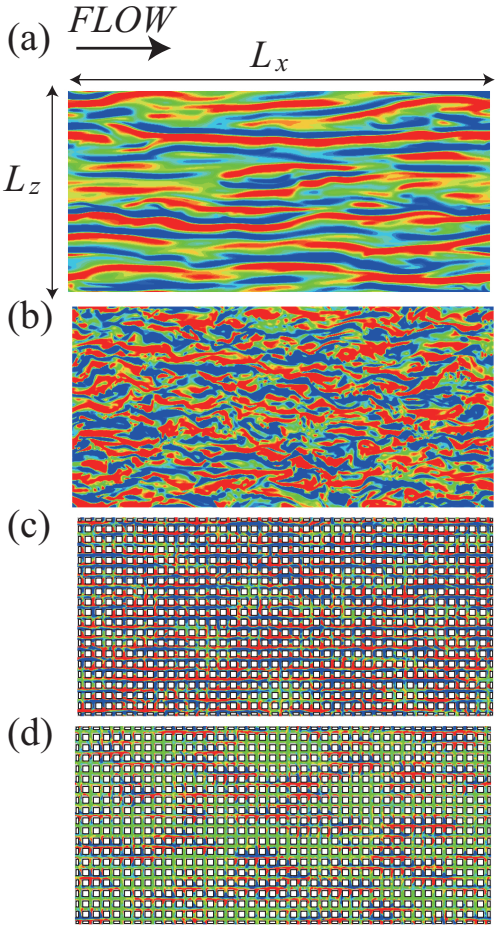

Figure 5. Wall-normal vorticity distributions; blue-red colours correspond to $-0.2 < \omega_y^{+} < 0.2$: (a) near the solid wall at $y'^{t+} = 11$, (b) near the porous layer at $y^{p+} = 10$, (c) at the interface of the porous layer, (d) inside the porous layer at $y^{p+} = -24$.

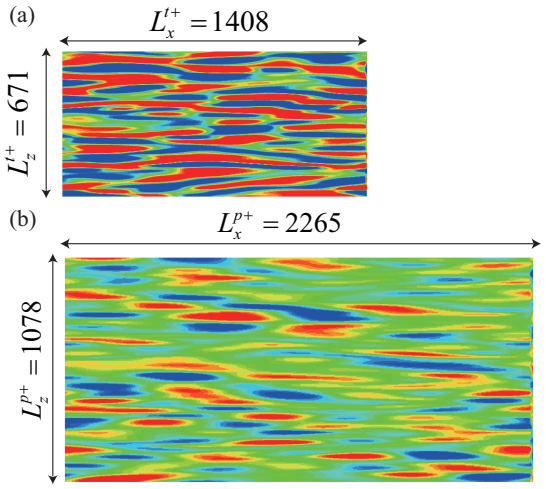

Figure 6. Low-pass filtered wall-normal vorticity distributions at $y^{p+}, y'^{t+} \simeq 10$; blue-red colours correspond to $-0.2 < \omega_y^+ < 0.2$: (a) near the solid wall, (b) near the porous layer.

In order to investigate the characteristic large scale vortex structures over the porous layer in detail, Figure 6 shows the snapshots of the low-pass filtered wall-normal vorticity. The vorticity is calculated by the low-pass filtered velocity fields where only the low wavenumber fluctuation velocity components of the span and streamwise directions ($\kappa_x, \kappa_z < 4/L_x$) are considered. Although the elongated streaky structure near the porous layer is hardly seen in figure 5, it is observed in the filtered wall-normal vorticity field. The streaky structure shown in figure 6 (b) seems to be wider in the spanwise and shorter in the streamwise directions compared with that near the solid wall of figure 6 (a).

To examine the scale of the vortex structure near the porous layer, figures 7 and 8 show the streamwise and spanwise autocorrelations at $y^{p+}, y'^{t+} \simeq 10$. From figure 7, the streamwise autocorrelations R_{uu}, R_{vv} and R_{ww} near the porous wall converge to zero faster than those near the solid wall. From the autocorrelation, the integral scale in the streamwise direction is computed as:

$$L^+_{u_iu_j} = \int_0^\infty R_{u_iu_j}(x^+)dx^+. \tag{7}$$

The integral scale of the streamwise velocity near the solid wall L_{uu}^{t+} and porous layer L_{uu}^{p+} are $L_{uu}^{t+} = 181, L_{uu}^{p+} = 87$, respectively and the L_{uu}^{p+} is found to be about a half of the L_{uu}^{t+}. The autocorrelations R_{vv} and R_{ww} near the porous layer have the local minimum whilst such tendency can not be seen near the solid wall. This implies that there exists the perturbation in the streamwise direction induced by the K-H instability and it is considered that this perturbation disrupts the elongated streaky structures near the porous layer. As seen in figure 8, the decay rates of the spanwise autocorrelations R_{uu}, R_{vv} and R_{ww} near the porous layer are smaller than those near the solid wall. Since the distance from the origin to the location of the local minimum of the autocorrelation R_{uu} corresponds to a half of the streak pitch, the streak pitch near the porous layer is approximately $L_{st}^{p+} \simeq 200$, which is approximately twice wider than that near the solid wall $L_{st}^{t+} \simeq 100$. Although the autocorrelations R_{uu} and R_{vv} near porous and solid walls have local minimum, the local minimum value near the solid wall is smaller than that near the porous layer. This implies that the streaky structure near the porous layer is more obscure than that near the solid wall. Above results mean that the streaky structure near the porous layer is approximately twice as wide as but half as long as that near the solid wall due to the large scale perturbation induced by the K-H instability. Hence the streaks become unclear compared with those near the solid wall, which corresponds to the observation in figures 5 and 6.

Figure 9 shows the one-dimensional energy spectra at $y^{p+}, y'^{t+} \simeq 10$. The energy density of the high wavenumbers are several orders lower than the energy density of the low wavenumber and the energy pile-up can not be seen in high wavenumber region. The streamwise and spanwise energy spectra of the wall-normal and spanwise components E_{vv}^+ and E_{ww}^+ are enhanced especially in the low wave number region ($\kappa_x^+, \kappa_z^+ < 0.1$). In particular, the spanwise en-

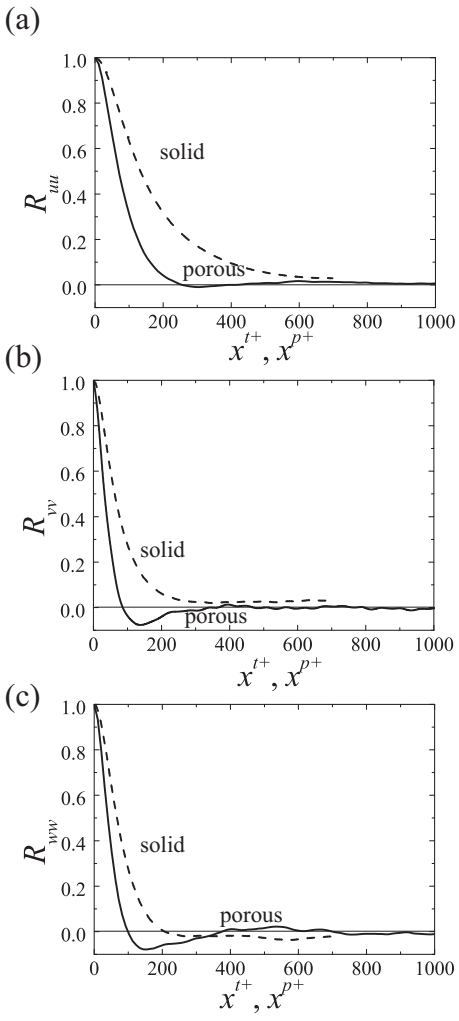

Figure 7. Streamwise autocorrelation profiles at $y^{p+}, y'^{t+} \simeq 10$: (a) R_{uu} along the streamwise direction, (b) R_{vv} along the streamwise direction, (c) R_{ww} along the streamwise direction.

ergy spectrum of the wall-normal component E^+_{vv} near the solid wall is damped due to the wall-blocking effect whilst that near the porous layer becomes significant and its level is approximately ten times larger than that near the solid wall. This means that the active injection and suction motions appears even near the porous layer. However the energy spectra of the wall-normal and spanwise components are enhanced, as shown in figure 9 (b) the spanwise energy spectrum of E^+_{uu} near the porous layer becomes larger in the low wavenumber region and smaller in the high wavenumber region. Therefore the energy spectra in the high wavenumber region become more isotropic than those near the solid wall. It is thus confirmed that although the elongated longitudinal structure near the porous wall is disrupted, the streamwise energy spectra E^+_{vv} and E^+_{ww} of the low wavenumber region don't decay and the levels of the energy densities become larger than those near the solid wall.

In order to investigate the effect of the pressure fluctuation, figure 10 shows the pressure fluctuation. The pressure fluctuation becomes significant near the interface of the porous layer. Although the pressure fluctuation rapidly decays inside the porous layer, it doesn't disappear even deep inside the porous layer and its level is roughly as the same as that near the solid wall. It is found that the effect of the pressure fluctuation exists even inside the porous layer.

For extracting the large scale pressure fluctuation induced by the K-H instability, the snapshot POD is applied to the pressure field. Figure 11 shows the POD modes of the pressure filed. It should be noted that the POD modes1

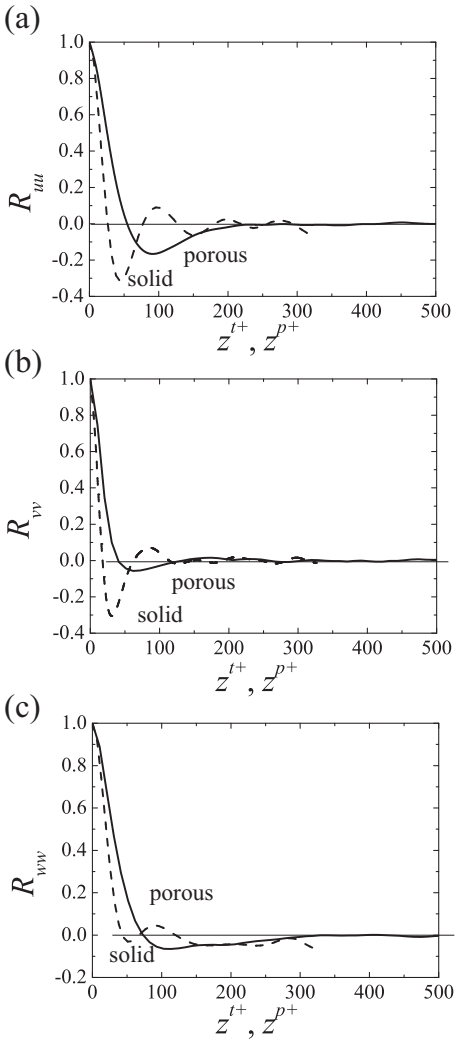

Figure 8. Spanwise autocorrelation profiles at y^{p+},$y^{t+} \simeq 10$: (a) R_{uu} along the streamwise direction, (b) R_{vv} along the streamwise direction, (c) R_{ww} along the streamwise direction.

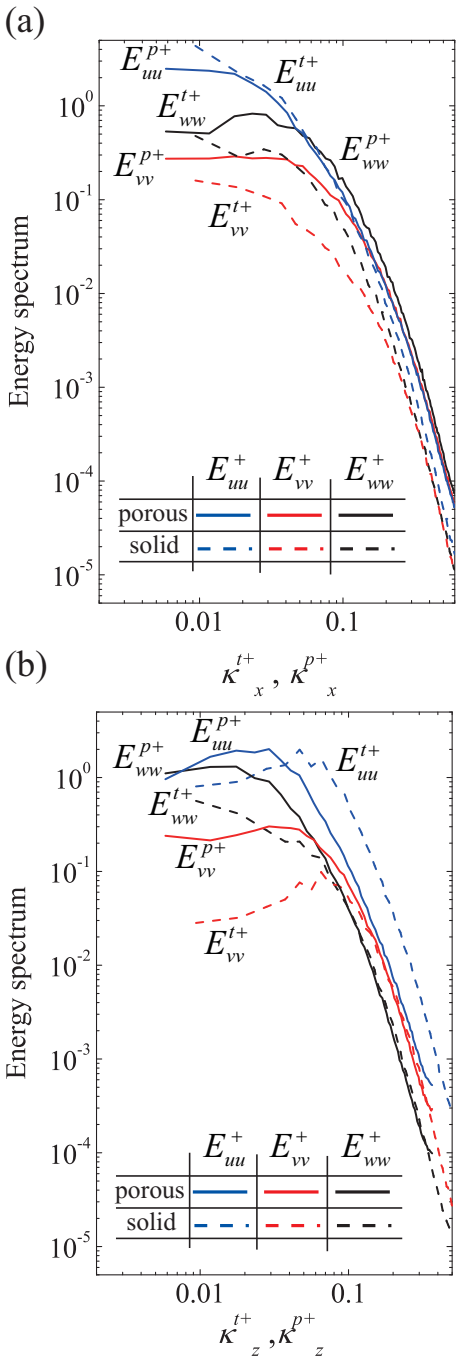

Figure 9. One-dimensional energy spectrum distributions at y^{p+},$y^{t+} \simeq 10$: (a) streamwise energy spectra, (b) spanwise energy spectra.

and 2, modes3 and 4, modes5 and 6 are the pair POD modes and each pair mode becomes the counterpart of each other. From figure 11, all POD modes shows the roll-cell structure stretched to the spanwise direction whose cores are regularly aliened over the porous layer. As the POD mode increases, the number of the roll-cell increases and the roll-cell structures prevail over the whole regions especially in the low-order modes. This large scale roll-cell structure is considered to come from the K-H instability and it is found that the effect of the K-H instability prevail not only in the clear channel region but also deep inside the porous layer.

CONCLUSION

A direct numerical simulation (DNS) study of a turbulent channel flow over a porous layer is performed by the D3Q27 multiple-relaxation time lattice Boltzmann method. The bulk Reynolds number is set to 3000 and the porous layer whose porosity is 0.71 consists of the staggered cube arrays. From the two-point autocorrelation, one-dimensional energy spectrum and proper orthogonal decomposition (POD) analyses, it is found that the streaky structure over the porous layer is disrupted by the large scale motion induced by the K-H instability. Autocorrelations reveal that the streak length becomes half and its width becomes twice of that near the solid wall. The large scale fluctuated motion is also detected by the one-dimensional spectrum analysis and the roll-cell structures in the pressure field by the K–H instability are revealed by the POD analysis. The Reynolds stress of the wall-normal component is significantly enhanced over the porous layer and it becomes the largest component inside the porous layer. This is because the perturbations by the K–H instability carry the turbulence vertically into the porous layer.

REFERENCES

Breugem, W. P., Boersma, B. J. and Uittenbogaard, R. E., 2006, "The influence of wall permeability on turbulent channel flow", J. Fluid Mech., Vol. 562, pp. 35-72.

Chandesris, M., D'Hueppe, A., Mathieu, B., Jamet, D. and B. Goyeau., 2013, " Direct numerical simulation of turbulent heat transfer in a fluid-porous domain", Phys. Fluid, 25, 125110.

Dupuis, A. and Chopard, B., 2003, "Theory and applications of an alternative lattice Boltzmann grid refinement algorithm", Phys. Rev. E, 67, 066707.

Suga, K., Matsumura, Y., Ashitaka, Y., Tominaga, S. and Kaneda, M., 2010, "Effects of wall permeability on turbulence", Int. J. Heat Fluid Flow, Vol. 31, pp. 974-984.

Suga, K., Mori, M. and Kaneda, M., 2011, "Vortex structure of turbulence over permeable walls", Int. J. Heat Fluid Flow, Vol. 32, pp. 586-595.

Suga, K., Kuwata, Y., Takashima,K. and Chikasue, R., 2015 "A D3Q27 Multiple-Relaxation-Time Lattice Boltzmann Method for Turbulent Flows", Compt. Math. Appl., Vol,69, pp. 518-529.

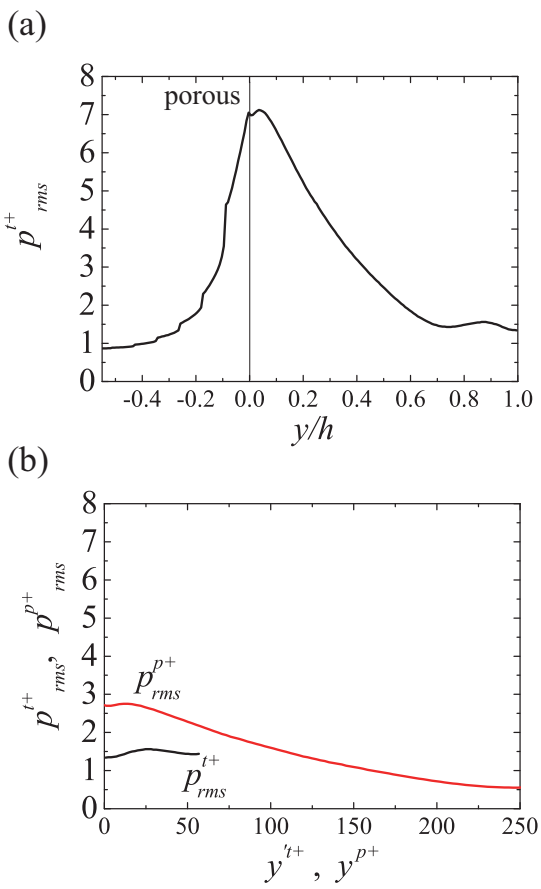

Figure 10. Pressure fluctuation profiles : (a) normalized profile by the solid wall friction velocity, (b) normalized profile by the friction velocity on each side.

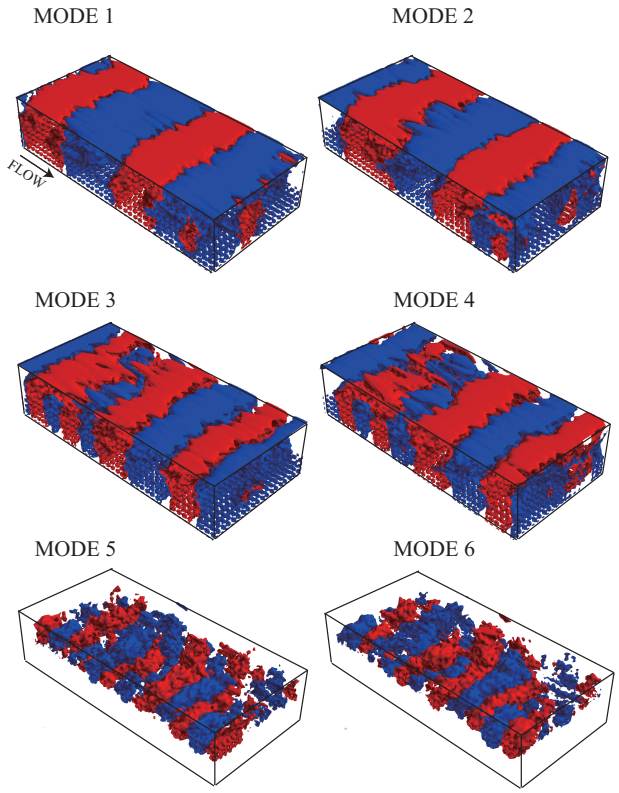

Figure 11. Snapshot POD modes of the pressure field.